Available online at www.sciencedirect.com

SCIENCE DIRECT®

ELSEVIER

Sensors and Actuators A 126 (2006) 33–40

SENSORS AND ACTUATORS A PHYSICAL

www.elsevier.com/locate/sna

Design and simulation of a dual-axis sensing decoupled vibratory wheel gyroscope☆

Deng-Horng Tsai, Weileun Fang*

Power Mechanical Engineering Department, National Tsing Hua University, 101 Kuang-Fu Road 2 Section, Hsinchu 30043, Taiwan

Received 12 January 2005; received in revised form 24 August 2005; accepted 2 September 2005
Available online 20 October 2005

Abstract

The current dual-axis vibratory wheel gyroscopes are mostly designed to have merely one proof mass, so the sensing signal measured from the two axes will interfere with each other and will result in zero rate output. This study presents a novel design of dual-axis sensing decoupled vibratory wheel gyroscope. The main structure, which consisted of three proof masses, can measure the angular rate of two different axes independently. A triple-beam-shape torsional spring is used to suppress the undesired in-plane linear motion of the proof mass. A prototype gyroscope design was employed to verify the concept and the performance of the present design concept. The simulation results show that the natural frequencies of the driving mode and the dual-axis sensing modes are 4585, 4604, and 4606 Hz, respectively. It successfully demonstrates that the dual-axis sensing modes are decoupled with each other. With the driving voltage of 20 V and the quality factor of 2000, the sensitivities of the dual-axis sensing modes can reach 7.4 and 19.4 fF/°/s, respectively, and the nonlinearity of the dual-axis sensing modes are only 0.04 and 0.29% within the dynamic range of ±150°/s.

Keywords: Dual-axis sensing decoupling; Vibratory wheel gyroscope; Zero rate output; Coriolis force

1. Introduction

Vibratory wheel gyroscopes have been studied extensively in the recent years [1–10]. They are different from the majority of the existing microgyroscopes based on either translational vibration [11] or structural mode vibration [12–14]. On the contrary, they will employ the rotational vibration to serve as the driving and the sensing modes.

According to the characteristics of mechanical coupling, the vibratory wheel gyroscopes can be classified into the coupled type [1–6] and the decoupled type [7–10]. The coupled type gyroscope has a single vibratory proof mass only. It is very often to exploit such a gyroscope to measure the dual-axis angular rates. Since the two out-of-plane sensing modes act on the single mass simultaneously, the sensing signal measured from the two axes will interfere with each other and will result in zero rate output. Unless the gyroscope adds on additional feedback detection and compensation circuit, the performance will not be improved to a great extent. As for the decoupled type gyroscope, it is characterized by two proof masses and can only detect the single-axis angular rate.

This research will present a novel dual-axis sensing decoupled vibratory wheel gyroscope. The presented design not only prevents the sensing coupled problem, but also provides the capability to measure the dual-axis angular rates. Besides, the triple-beam-shape torsional spring will be used to suppress the mechanical noise from the undesired in-plane motion of the proof mass.

2. Gyroscope design

In order to achieve the dual-axis sensing decoupling, the main structure of the present vibratory wheel gyroscope will be designed to comprise three inertia components. The design methodology, operating principle, mathematical model governing dynamic characteristics, dc frequency tuning and how to suppress the mechanical noise of the gyroscope will be studied.

2.1. Basic operating principle

Fig. 1a shows the illustration of the vibratory wheel gyroscope. The main structure is consisted of three movable inertia

☆APCOT-MNT 2004: Asia-Pacific Conference on Transducers and Micro-Nano Technology, Sapporo, 4–7 July 2004.

* Corresponding author. Tel.: +886 3 574 2923;
fax: +886 3 573 9372/572 2840.
E-mail address: fang@pme.nthu.edu.tw (W. Fang).

0924-4247/$ – see front matter © 2005 Elsevier B.V. All rights reserved.
doi:10.1016/j.sna.2005.09.004

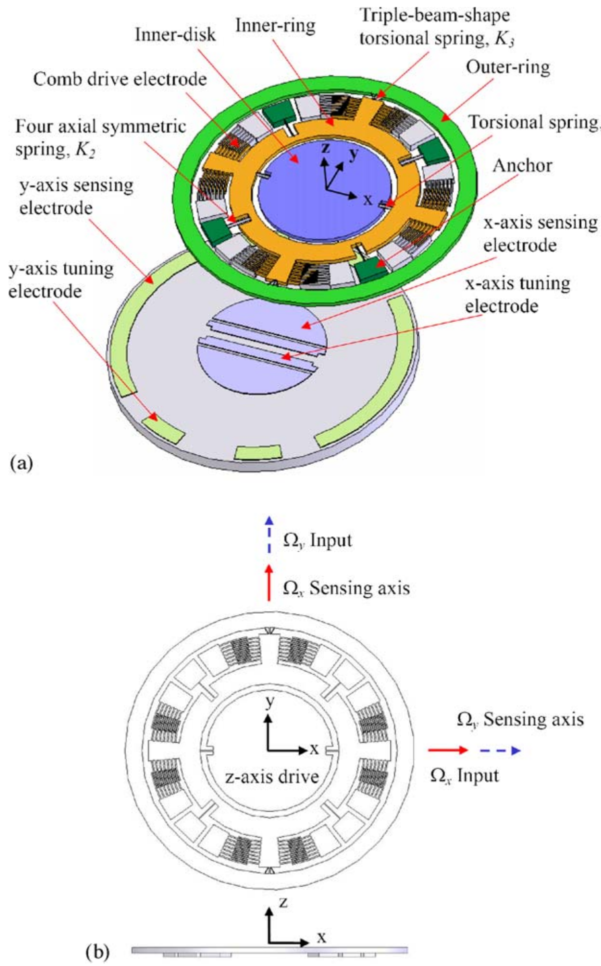

Fig. 1. The schematic illustration of (a) the present vibratory wheel gyroscope, and (b) its operating mechanism.

components (i.e. proof mass), such as an inner-ring, an outer-ring, and an inner-disk. The inner-ring is suspended by four axial symmetric springs, K_2, which anchored to the substrate. These springs provide an equivalent rotational stiffness to the inner-ring during the driving mode. The inner-disk is connected to the inner-ring by torsion spring K_1. The torsional spring K_1 is designed to allow the inner-disk only rotate about the *x*-axis. In addition, the outer-ring is connected to the inner-ring by the triple-beam-shape torsion spring K_3. The outer-ring can only rotate about the *y*-axis due to the constraint of the torsional spring K_3. The detailed operating mechanism of the presented gyroscope can be shown in Fig. 1b. This study employed the inner-ring as the driving element and the inner-disk and the outer-ring as the sensing elements. All of these three inertia components will rotate about the *z*-axis when the inner-ring is driven by the comb electrodes. In this study, the springs K_1 and K_3 were designed to have large in-plane bending stiffness, so that the inner-ring, the inner-disk, and the outer-ring had the same in-plane angular displacement. Moreover, these three proof masses are operating at their angular resonant frequency to provide driving mode. Once the gyroscope experiences an angular rate in *y*-axis, the inner-disk will vibrate angularly about the *x*-axis due to the Coriolis force. If the gyroscope detects an angular rate in *x*-axis, the outer-ring will also vibrate angularly about the *y*-axis due to the Coriolis force. By this way, the dual-axis sensing decoupling gyroscope is realized.

2.2. Mathematical model

In this subsection, the mathematical model has been established from the dynamics of the dual-axis sensing decoupled vibratory gyroscope. Euler angles are adopted to characterize the position of three inertia components of the gyroscope at any instant. Let θ_z be the angular displacement of the three masses about the *z*-axis and an external angular rate Ω_x is imposed on the gyroscope. According to the Coriolis forces, the outer-ring rotates through an angle ϕ_y about the *y*-axis, in the meanwhile, the inner-ring and the inner-disk rotate through a smaller angle $\phi_{y'}$ about the *y*-axis due to the stronger support by four axial symmetric springs. Fig. 2a shows the angular displacement associated with the input excitation of Ω_x. The angular velocity of the outer-ring can be expressed as

$$\begin{aligned}\tilde{\omega}_{3x} &= \dot{\phi}_y \sin\theta_z + \Omega_x \cos\phi_y \cos\theta_z,\\ \tilde{\omega}_{3y} &= \dot{\phi}_y \cos\theta_z - \Omega_x \cos\phi_y \sin\theta_z,\\ \tilde{\omega}_{3z} &= \dot{\theta}_z - \Omega_x \sin\phi_y \qquad (1)\end{aligned}$$

where $\tilde{\omega}_{ij}$ ($i = 1, 2, 3$, and $j = x, y, z$) represents the angular velocity of the three inertias. The double subscript notation is interpreted as follows: the first subscript *i* indicates the angular velocity for the inner-disk ($i = 1$), the inner-ring ($i = 2$) and the

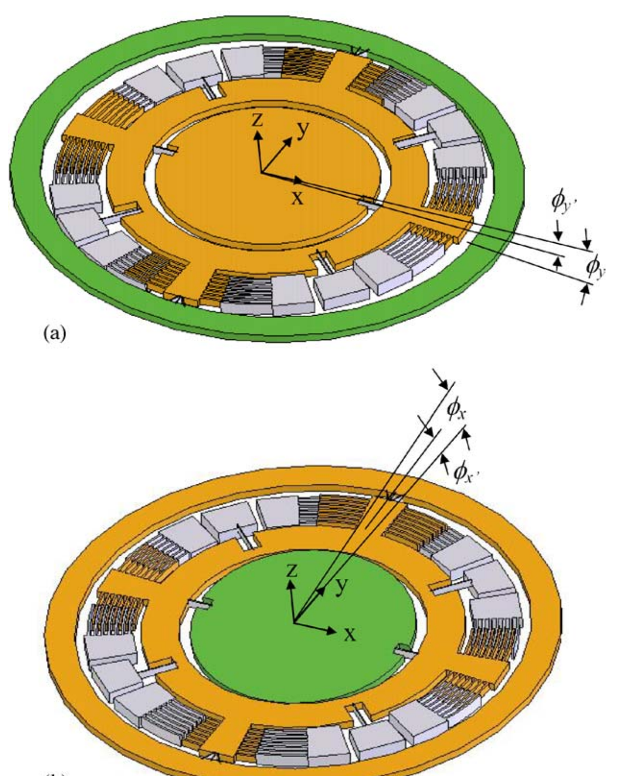

Fig. 2. Angular displacement associated with (a) the Ω_x input, and (b) the Ω_y input.

outer-ring ($i = 3$), respectively; the second subscript j indicates the directions of the angular velocity

$$\tilde{\omega}_{ix} = \dot{\phi}_{y'} \sin\theta_z + \Omega_x \cos\phi_{y'} \cos\theta_z,$$
$$\tilde{\omega}_{iy} = \dot{\phi}_{y'} \cos\theta_z - \Omega_x \cos\phi_{y'} \sin\theta_z,$$
$$\tilde{\omega}_{iz} = \dot{\theta}_z - \Omega_x \sin\phi_{y'}, \quad i = 1, 2 \tag{2}$$

Similarly, the angular displacements associated with the input excitation of Ω_y are illustrated in Fig. 2b. According to the Coriolis forces, the inner-disk rotates through an angle ϕ_x about the x-axis; meantime, the inner-ring and the outer-ring also rotate through a smaller angle $\phi_{x'}$ about the x-axis due to the stiff support by four axial symmetric springs. The angular velocity of the inner-disk can be expressed as

$$\tilde{\omega}_{1x} = \dot{\phi}_x \cos\theta_z + \Omega_y \cos\phi_x \sin\theta_z,$$
$$\tilde{\omega}_{1y} = -\dot{\phi}_x \sin\theta_z + \Omega_y \cos\phi_x \cos\theta_z,$$
$$\tilde{\omega}_{1z} = \dot{\theta}_z - \Omega_y \sin\phi_x \tag{3}$$

The angular velocity $\tilde{\omega}_{ij}$ of the inner-ring ($i = 2$) and the outer-ring ($i = 3$) also can be written as

$$\tilde{\omega}_{ix} = \dot{\phi}_{x'} \cos\theta_z + \Omega_y \cos\phi_{x'} \sin\theta_z,$$
$$\tilde{\omega}_{iy} = -\dot{\phi}_{x'} \sin\theta_z + \Omega_y \cos\phi_{x'} \cos\theta_z,$$
$$\tilde{\omega}_{iz} = \dot{\theta}_z - \Omega_y \sin\phi_{x'}, \quad i = 2, 3 \tag{4}$$

When the gyroscope experiences the angular rates of Ω_x and Ω_y simultaneously, the angular velocity $\tilde{\omega}_{ij}$ of the inner-disk ($i = 1$), the inner-ring ($i = 2$) and the outer-ring ($i = 3$) became

$$\tilde{\omega}_{1x} = \dot{\phi}_x + \Omega_y\theta_z + \dot{\phi}_{y'}\theta_z + \Omega_x,$$
$$\tilde{\omega}_{1y} = -\dot{\phi}_x\theta_z + \Omega_y + \dot{\phi}_{y'} - \Omega_x\theta_z,$$
$$\tilde{\omega}_{1z} = \dot{\theta}_z - \Omega_y\phi_x - \Omega_x\phi_{y'} \tag{5}$$

$$\tilde{\omega}_{2x} = \dot{\phi}_{x'} + \Omega_y\theta_z + \dot{\phi}_{y'}\theta_z + \Omega_x,$$
$$\tilde{\omega}_{2y} = -\dot{\phi}_{x'}\theta_z + \Omega_y + \dot{\phi}_{y'} - \Omega_x\theta_z,$$
$$\tilde{\omega}_{2z} = \dot{\theta}_z - \Omega_y\phi_{x'} - \Omega_x\phi_{y'} \tag{6}$$

$$\tilde{\omega}_{3x} = \dot{\phi}_y\theta_z + \Omega_x + \dot{\phi}_{x'} + \Omega_y\theta_z,$$
$$\tilde{\omega}_{3y} = \dot{\phi}_y - \Omega_x\theta_z - \dot{\phi}_{x'}\theta_z + \Omega_y,$$
$$\tilde{\omega}_{3z} = \dot{\theta}_z - \Omega_x\phi_y - \Omega_y\phi_{x'} \tag{7}$$

In this case, the angular displacements of θ_z, ϕ_x, $\phi_{x'}$, ϕ_y and $\phi_{y'}$ are assumed to be small quantities. The kinetic energy T of the gyroscope is

$$T = \frac{1}{2}(J_{ix}\tilde{\omega}_{ix}^2 + J_{iy}\tilde{\omega}_{iy}^2 + J_{iz}\tilde{\omega}_{iz}^2), \quad i = 1, 2, 3 \tag{8}$$

where J_{ij} ($i = 1$, 2, 3, and $j = x$, y, z) represents the moment of inertia of the three masses. The double subscript notation is interpreted as follows: the first subscript i indicates the moment of inertia for the inner-disk ($i = 1$), the inner-ring ($i = 2$) and the outer-ring ($i = 3$), respectively; the second subscript j indicates the moment of inertia about the x, y, and z axes, respectively.

While the potential energy V of the gyroscope and the energy dissipation D due to damping in the system are given as

$$V = \frac{1}{2}K_{2z}\theta_z^2 + \frac{1}{2}K_{1x}(\phi_x - \phi_{x'})^2 + \frac{1}{2}K_{2x}\phi_{x'}^2 + \frac{1}{2}K_{3y}(\phi_y - \phi_{y'})^2 + \frac{1}{2}K_{2y}\phi_{y'}^2 \tag{9}$$

$$D = \frac{1}{2}(C_{1z} + C_{2z} + C_{3z})\dot{\theta}_z^2 + \frac{1}{2}C_{1x}\dot{\phi}_x^2 + \frac{1}{2}(C_{2x} + C_{3x})\dot{\phi}_{x'}^2 + \frac{1}{2}C_{3y}\dot{\phi}_y^2 + \frac{1}{2}(C_{1y} + C_{2y})\dot{\phi}_{y'}^2 \tag{10}$$

where K_{2j} ($j = x$, y, z) are the net equivalent rotational spring constants of the spring K_2, as illustrated in Fig. 1a, about the x-, y- and z-directions, respectively. The spring K_{1x} is the net equivalent torsional spring constant of the spring K_1 about the x-directions, and the spring K_{3y} is the net equivalent torsional spring constant of the spring K_3 about y-directions. Again, C_{ij} ($i = 1$, 2, 3, and $j = x$, y, z) are the damping coefficients of the inner-disk ($i = 1$), the inner-ring ($i = 2$) and the outer-ring ($i = 3$), in the x-, y- and z-directions, respectively. The motion equation of the driving mode can be written as

$$\frac{\mathrm{d}}{\mathrm{d}t}\left(\frac{\partial T}{\partial \dot{\theta}_z}\right) - \frac{\partial T}{\partial \theta_z} + \frac{\partial V}{\partial \theta_z} + \frac{\partial D}{\partial \dot{\theta}_z} = M \tag{11}$$

where M is the moment supplied by the comb drive electrodes. The motion equations of the dual-axis sensing modes can be derived. Assume Ω_x and Ω_y to be small, and the higher order terms of Ω_x, Ω_y, and θ_z are negligible. Finally, the motion equations of the driving mode and the sensing mode about each sensing axis can be expressed as

$$\begin{aligned}(J_{1z} + J_{2z} + J_{3z})\ddot{\theta}_z &+ (C_{1z} + C_{2z} + C_{3z})\dot{\theta}_z + K_{2z}\theta_z \\ &= M + (J_{1z}\dot{\phi}_{y'} + J_{2z}\dot{\phi}_{y'} + J_{3z}\dot{\phi}_y)\Omega_x \\ &+ (J_{1z}\dot{\phi}_x + J_{2z}\dot{\phi}_{x'} + J_{3z}\dot{\phi}_{x'})\Omega_y\end{aligned} \tag{12}$$

$$\begin{bmatrix} J_{2x} + J_{3x} & 0 \\ 0 & J_{1x} \end{bmatrix}\begin{Bmatrix} \ddot{\phi}_{x'} \\ \ddot{\phi}_x \end{Bmatrix} + \begin{bmatrix} C_{2x} + C_{3x} & 0 \\ 0 & C_{1x} \end{bmatrix}\begin{Bmatrix} \dot{\phi}_{x'} \\ \dot{\phi}_x \end{Bmatrix} + \begin{bmatrix} K_{1x} + K_{2x} & -K_{1x} \\ -K_{1x} & K_{1x} \end{bmatrix}\begin{Bmatrix} \phi_{x'} \\ \phi_x \end{Bmatrix} = \begin{Bmatrix} -(J_{2z} + J_{3z})\dot{\theta}_z\Omega_y \\ -J_{1z}\dot{\theta}_z\Omega_y \end{Bmatrix} \tag{13}$$

$$\begin{bmatrix} J_{1y} + J_{2y} & 0 \\ 0 & J_{3y} \end{bmatrix}\begin{Bmatrix} \ddot{\phi}_{y'} \\ \ddot{\phi}_y \end{Bmatrix} + \begin{bmatrix} C_{1y} + C_{2y} & 0 \\ 0 & C_{3y} \end{bmatrix}\begin{Bmatrix} \dot{\phi}_{y'} \\ \dot{\phi}_y \end{Bmatrix} + \begin{bmatrix} K_{3y} + K_{2y} & -K_{3y} \\ -K_{3y} & K_{3y} \end{bmatrix}\begin{Bmatrix} \phi_{y'} \\ \phi_y \end{Bmatrix} = \begin{Bmatrix} -(J_{1z} + J_{2z})\dot{\theta}_z\Omega_x \\ -J_{3z}\dot{\theta}_z\Omega_x \end{Bmatrix} \tag{14}$$

The terms on the right-hand side of Eqs. (13) and (14) represent the Coriolis forces, which result from the input angular rates Ω_y

and Ω_x. It indicates that there are no identical elements in the mass matrix, damping matrix, stiffness matrix, and force vector between Eqs. (13) and (14). In other words, the dual-axis sensing modes are decoupled. Thus, the cross axis sensitivity between the dual-axis sensing modes should be zero.

2.3. Resonant frequency design

The frequency of the gyroscope associated with the driving mode (in z-direction) is given by

$$\omega_z = \sqrt{\frac{K_{2z}}{J_{1z}+J_{2z}+J_{3z}}} \tag{15}$$

After the spring constant K_{2z} determined by Eq. (15), the spring constants K_{2x} and K_{2y} contributed by spring K_2 also can be obtained. According to Eqs. (13) and (14), the resonant frequencies associated with the dual-axis sensing modes ω_x and ω_y are expressed as

$$\omega_x = \sqrt{\frac{\omega_1^2+\omega_2^2-\sqrt{(\omega_1^2+\omega_2^2)^2+4\omega_2^2\frac{J_{1x}}{J_{2x}+J_{3x}}}}{2}} \tag{16}$$

$$\omega_y = \sqrt{\frac{\omega_3^2+\omega_4^2-\sqrt{(\omega_3^2+\omega_4^2)^2+4\omega_4^2\frac{J_{3y}}{J_{1y}+J_{2y}}}}{2}} \tag{17}$$

where

$$\omega_1 = \sqrt{\frac{K_{1x}+K_{2x}}{J_{2x}+J_{3x}}}, \qquad \omega_2 = \sqrt{\frac{K_{1x}}{J_{1x}}},$$

$$\omega_3 = \sqrt{\frac{K_{3y}+K_{2y}}{J_{1y}+J_{2y}}}, \qquad \omega_4 = \sqrt{\frac{K_{3y}}{J_{3y}}}$$

Then, from Eqs. (16) and (17), the spring constants K_{1x} and K_{3y} could be designed to enable the frequencies of the dual-axis sensing modes approaching to that of the driving mode. Meanwhile, the higher resonant frequencies $\omega_{x'}$ and $\omega_{y'}$ associated with Eqs. (13) and (14), respectively, should be large enough to decouple with the lower dual-axis sensing frequencies of ω_x and ω_y.

2.4. dc frequency tuning

The material properties as well as the dimensions of the gyroscope may deviate from the designed values due to fabrication error. These errors will cause frequency mismatching of the device and reduce its performance. In order to increase the sensitivity of gyroscope, the dc bias voltage of the tuning electrodes is exploited to generate the electrostatic negative stiffness [15]. As indicated in Fig. 1a, these negative springs resulted from the x-axis and y-axis tuning electrodes will be employed to tune the resonant frequencies of ω_x and ω_y, respectively. To this end, an equivalent torsional negative stiffness K_{ex} about x-axis associated with the dc bias voltage V_{dc} can be expressed as

$$K_{ex} = \frac{4\varepsilon A y_c V_{dc}^2}{d^3} \tag{18}$$

where ε is the permittivity of air, A the area of the tuning electrode, y_c the distance from the tuning electrode center to the x-axis, and d is the gap between the device structure and the tuning electrode. Consequently, the tuned stiffness K_{t1x} and the tuned resonant frequency in the x-axis ω_{tx} are

$$K_{t1x} = K_{1x} - K_{ex} \tag{19}$$

$$\omega_{tx} = \sqrt{\frac{\omega_{t1}^2+\omega_{t2}^2-\sqrt{(\omega_{t1}^2+\omega_{t2}^2)^2+4\omega_{t2}^2\frac{J_{1x}}{J_{2x}+J_{3x}}}}{2}} \tag{20}$$

where

$$\omega_{t1} = \sqrt{\frac{K_{t1x}+K_{2x}}{J_{2x}+J_{3x}}}, \qquad \omega_{t2} = \sqrt{\frac{K_{t1x}}{J_{1x}}}$$

Similarly, an equivalent torsional negative stiffness K_{ey} was contributed by y-axis tuning electrodes associated with the dc bias voltage V_{dc}. The stiffness K_{3y} and the resonant frequency ω_y can be tuned through the same manner.

2.5. Triple-beam-shape torsional spring

The outer-ring has larger mass and longer supported span than the inner-disk. Therefore, it is much easy to be excited by the external disturbance and produces unexpected motion, such as in-plane vibration in the x-direction. In order to suppress the undesired motion of the outer-ring, the triple-beam-shape torsional spring schematic illustrated in the inset of Fig. 3a is designed. In this design, the y-axis torsional stiffness and the x-axis in-plane linear stiffness can be tuned by the oblique angle θ. Thus, the frequencies of the y-axis torsional vibration and the x-axis in-plane linear motion also can be tuned by the oblique angle.

Using commercial FEM software, the relationship between the torsional frequency ω_y, the in-plane motion frequency ω_{x0} and the oblique angle θ are simulated. The typical simulation results in Fig. 3a show the variation of ω_y and ω_{x0} with the oblique angle θ. Apparently, the larger the oblique angle θ is, the higher the two frequencies ω_y and ω_{x0} will become. But Fig. 3b shows that the triple-beam-shape torsional spring for $\theta = 30°$ has the maximum frequency ratio of ω_{x0} to ω_y, so it has the highest stiffness to resist the in-plane motion under the same torsional stiffness. In other words, the triple-beam-shape torsional spring has an optimal design for $\theta = 30°$ to suppress the undesired mechanical noise induced by the x-axis in-plane linear motion.

3. Performance analysis

To verify the concept and the performance of the present gyroscope, the dimensions of a typical prototype design were listed in Table 1. Fig. 4 shows the first three vibration modes of the gyroscope from ANSYS simulation. The natural frequencies of the driving mode and the dual-axis sensing modes are 4585, 4604 and 4606 Hz, respectively. During the driving mode, the three proof masses experience in-plane rigid-body angular oscillation yet the springs K_2 have in-plane transverse vibration. During the dual-axis sensing modes, the inner-disk and the outer-ring perform the out-of-plane torsional oscillation, respectively. It

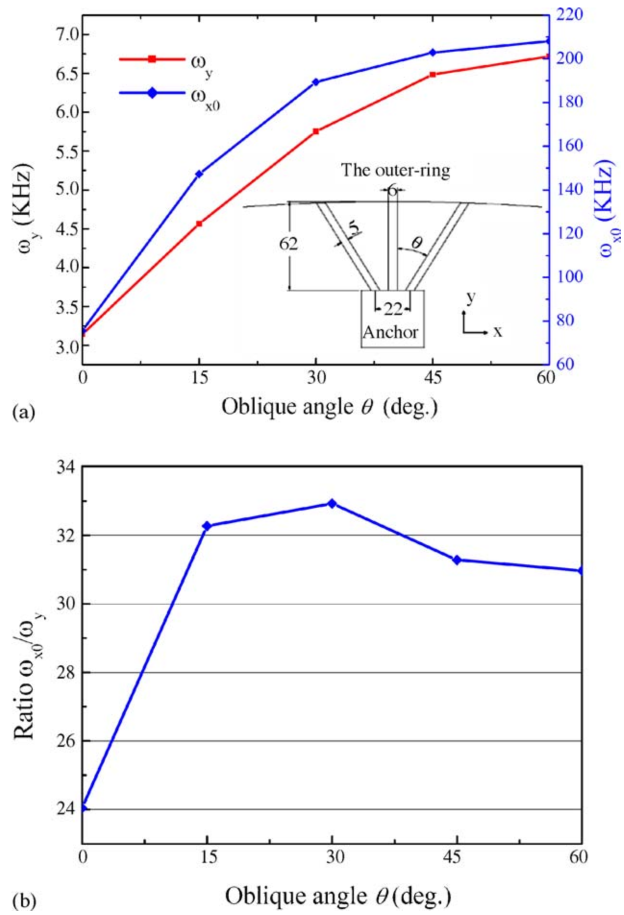

Fig. 3. Relationship between (a) ω_y, ω_{x0} and oblique angle θ, and (b) frequency ratio and oblique angle θ.

once again successfully demonstrates that the dual-axis sensing modes are decoupled with each other. The resonant frequencies of dual-axis sensing modes are designed to be higher than that of the driving mode, so as to enable the frequency matching after the dc frequency tuning [16]. Fig. 5 shows the tuned resonant frequencies of the dual-axis sensing modes as a function of the dc bias voltage. In this case, the gap d is 2 μm and the area A is 105 000 μm^2. According to Eqs. (18)–(20), it required the dc voltages of 42 and 54 V, respectively, as indicated in Fig. 5, to tune the frequencies of the dual-axis sensing modes to be identical with the driving one. The performances of the gyroscope

Table 1
Values for geometrical design parameters

Design parameter	Value (μm)
Inner-disk radius	600
Inner-ring inner radius	660
Inner-ring outer radius	860
Outer-ring inner radius	1210
Outer-ring outer radius	1370
Structural layer thickness	25
Axial symmetric spring length	220
Axial symmetric spring width	5
Torsional spring length	125
Torsional spring width	8
Triple-beam-shape torsional spring dimensions	As in Fig. 3a

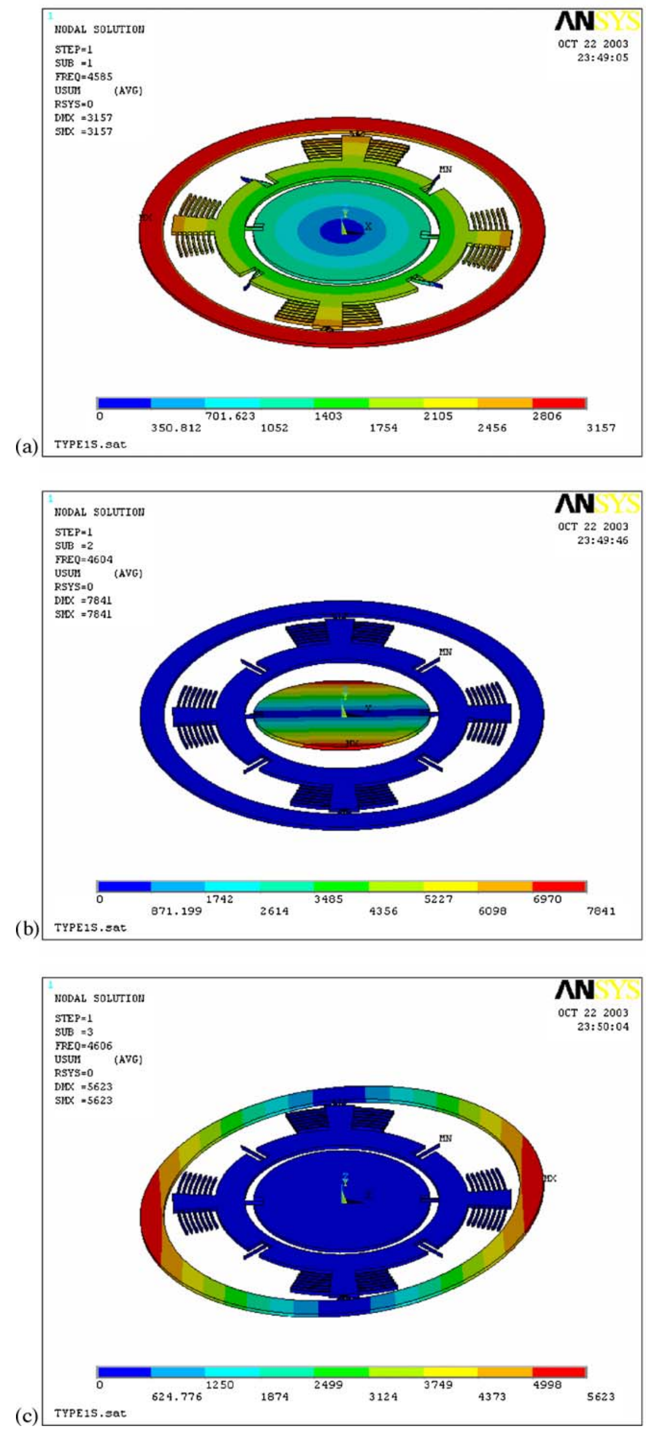

Fig. 4. FEM modal analysis of the gyroscope: (a) in-plane mode of three proof masses, (b) out-of-plane mode of the inner-disk, and (c) out-of-plane mode of the outer-ring.

will be further evaluated based on the nonlinearity and sensitivity analysis.

3.1. Nonlinearity analysis

From Eq. (12), the excitations include not only the torque M provided by the comb drive electrode but also six additional terms. These six terms resulted from the interaction of Ω_x and

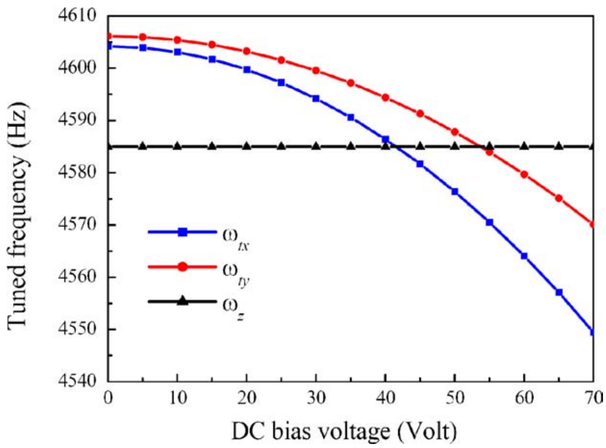

Fig. 5. Variation of the tuned resonant frequencies with the dc bias voltage.

Ω_y, with the angular velocities of proof masses caused by the dual-axis sensing modes in Eqs. (13) and (14). However, these six terms and the torque M applied in the opposite directions. In addition, the magnitudes of these six terms were rather small; the stability of the gyroscope will not be influenced. Nevertheless, these six terms affected the amplitude of the driving mode and indirectly caused the nonlinearity of the dual-axis sensing modes. As a typical study case, the driving voltage of 20 V and the quality factor Q of 2000 were used in the model. From Eqs. (12)–(14), the relationship between the amplitude of θ_z and Ω_x and Ω_y was analyzed, as shown in Fig. 6a. The influence of θ_z on the nonlinearity of the dual-axis sensing modes was also predicted, as shown in Fig. 6b. The induced nonlinearities for the dual-axis sensing modes were 0.29 and 0.04%, respectively within the sensing range of $\pm 150°$/s.

3.2. Sensitivity

The sensitivity of the gyroscope is expressed in terms of the Coriolis oscillation rotational angle ϕ_x (or ϕ_y) per input angular rate Ω_y (or Ω_x). The sensitivity can be derived from Eqs. (13) and (14) with the final form

$$\frac{\phi_x}{\Omega_y}=\left|\frac{-(1-r_1^2\beta_{x'}^2+\mathrm{j}2r_1^2\beta_{x'}\zeta_{x'})\frac{J_{1z}\dot{\theta}_z}{K_{t1x}}-\frac{(J_{2z}+J_{3z})\dot{\theta}_z}{K_{t1x}+K_{2x}}}{(1-r_1^2\beta_{x'}^2+\mathrm{j}2r_1^2\beta_{x'}\zeta_{x'})(1-r_2^2\beta_x^2+\mathrm{j}2r_2^2\beta_x\zeta_x)-\frac{K_{t1x}}{K_{t1x}+K_{2x}}}\right| \tag{21}$$

$$\frac{\phi_y}{\Omega_x}=\left|\frac{-(1-n_1^2\beta_{y'}^2+\mathrm{j}2n_1^2\beta_{y'}\zeta_{y'})\frac{J_{3z}\dot{\theta}_z}{K_{t3y}}-\frac{(J_{1z}+J_{2z})\dot{\theta}_z}{K_{t3y}+K_{2y}}}{(1-n_1^2\beta_{y'}^2+\mathrm{j}2n_1^2\beta_{y'}\zeta_{y'})(1-n_2^2\beta_y^2+\mathrm{j}2n_2^2\beta_y\zeta_y)-\frac{K_{t3y}}{K_{t3y}+K_{2y}}}\right| \tag{22}$$

where

$$r_1=\frac{\omega_{tx'}}{\omega_{t1}},\qquad r_2=\frac{\omega_{tx}}{\omega_{t2}},\qquad n_1=\frac{\omega_{ty'}}{\omega_{t3}},\qquad n_2=\frac{\omega_{ty}}{\omega_{t4}},$$

$$\beta_x=\frac{\omega_d}{\omega_{tx}},\qquad \beta_{x'}=\frac{\omega_d}{\omega_{tx'}},\qquad \beta_y=\frac{\omega_d}{\omega_{ty}},\qquad \beta_{y'}=\frac{\omega_d}{\omega_{ty'}},$$

$$\zeta_{x'}=\frac{C_{2x}+C_{3x}}{2(J_{2x}+J_{3x})\omega_{tx'}},\qquad \zeta_x=\frac{C_{1x}}{2J_{1x}\omega_{tx}},$$

$$\zeta_{y'}=\frac{C_{1y}+C_{2y}}{2(J_{1y}+J_{2y})\omega_{ty'}},\qquad \zeta_y=\frac{C_{3y}}{2J_{3y}\omega_{ty}}$$

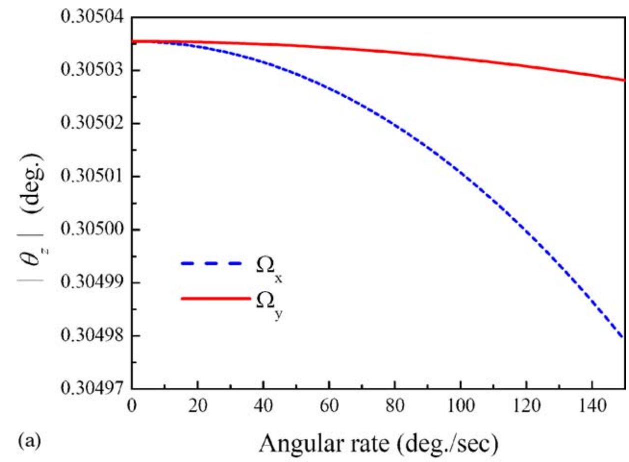

(a)

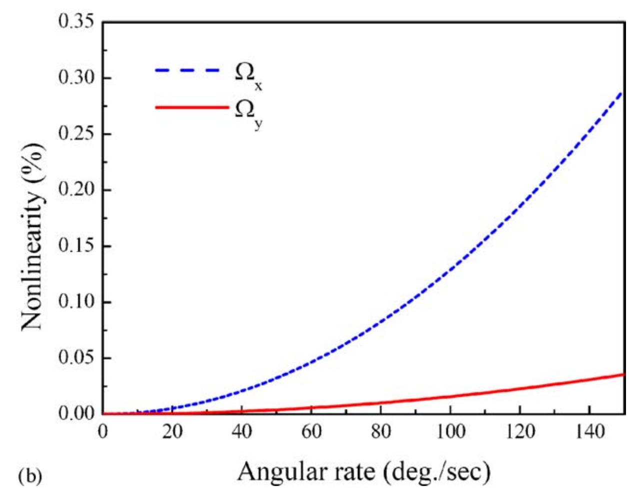

(b)

Fig. 6. (a) Relationship between the amplitude of θ_z and the angular rate inputs Ω_x and Ω_y, and (b) nonlinearity for the dual-axis sensing modes.

where K_{t3y} is the tuned stiffness in the y-axis, ω_d is the driving frequency of the comb drive electrode, $\omega_{tx'}$, ω_{ty}, $\omega_{ty'}$, ω_{t3} and ω_{t4} are tuned resonant frequencies by dc bias voltage, r_1, r_2, n_1, n_2, β_x, $\beta_{x'}$, β_y and $\beta_{y'}$ are frequency ratios. The parameters $\zeta_{x'}$, ζ_x, $\zeta_{y'}$ and ζ_x are damping ratios which are equal to $1/(2Q)$.

The rotational vibration due to the Coriolis force can be determined by measuring the capacitance change of the sensing electrodes indicated in Fig. 1a. Fig. 7 further shows the differential sensing design of these electrodes. Thus, the capacitance changes of ΔC_x and ΔC_y of the dual-axis sensing modes are expressed as

$$\Delta C_x=\frac{4\varepsilon\phi_x}{3d^2}(R_1^2-W_1^2)^{3/2} \tag{23}$$

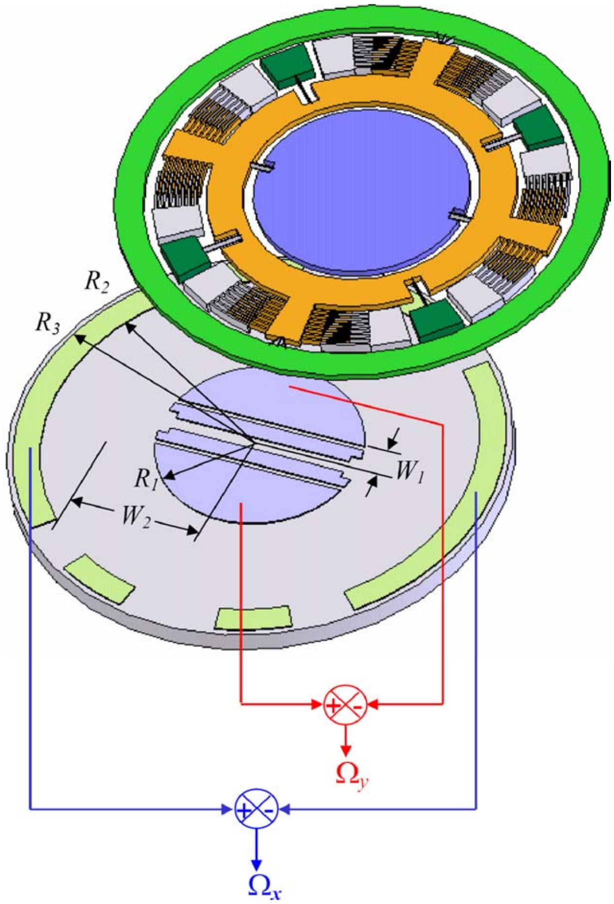

Fig. 7. Differential sensing of the dual-axis.

$$\Delta C_y = \frac{4\varepsilon\phi_y}{3d^2}[(R_3^2 - W_2^2)^{3/2} - (R_2^2 - W_2^2)^{3/2}] \tag{24}$$

As indicated in Fig. 7, R_1 is the radius of the x-axis sensing electrode, R_2 and R_3 are the inner and outer radius of the y-axis sensing electrode, and W_1 and W_2 are the nearest distances from the dual-axis sensing electrodes to the rotational axes.

The variation of the sensitivity with the frequencies ratio, ω_d/ω_{tx} and ω_d/ω_{ty}, and quality factor Q are shown in Figs. 8 and 9, respectively. When the driving frequency of the comb electrodes is the same as the frequencies of the dual-axis sensing modes, the maximum sensitivity can be obtained. Besides, increasing the quality factor can also be applied to improve the sensitivity of the gyroscope. Tables 2 and 3 have summarized the characteristics of the driving mode and the dual-axis sensing modes, respectively. Table 3 also shows that the rotational angle sensitivities of the dual-axis sensing modes are very close. The outer-ring has a larger radius, so its capacitance sensitivity is higher than that of the inner-disk. This study also employed the ANSYS simulation to further verify the results predicted from mathematical model. According to the ANSYS harmonic analysis, the sensitivities of the Ω_x and Ω_y sensing modes were 0.018 and 0.0078 μm/°/s, respectively. The results determined from ANSYS harmonic analysis are in good agreement with those from mathematical model.

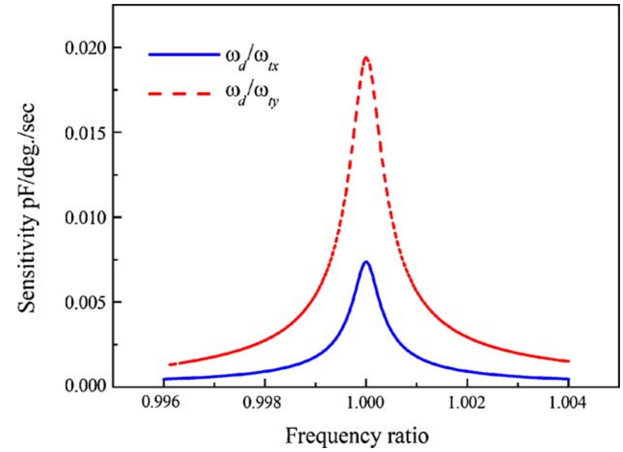

Fig. 8. Variation of the sensitivity with the frequency ratio.

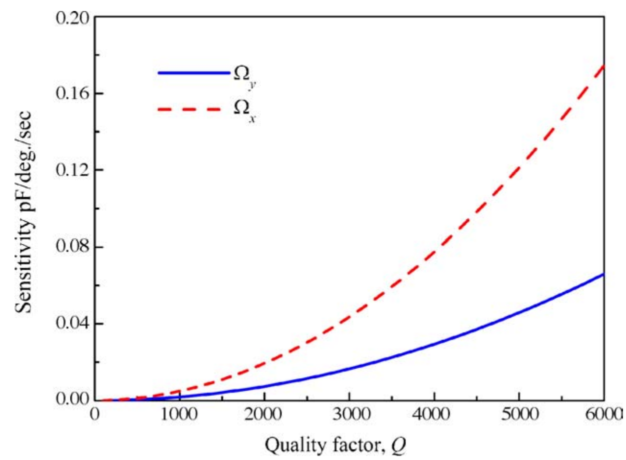

Fig. 9. Variation of the sensitivity with the quality factor.

Table 2
The characteristics of the driving mode and the associated driving conditions

Design parameter	Value
Quality factor, Q	2000
Natural frequency, ω_z (Hz)	4585
Drive voltage, V_{drive} (V)	20
Drive torque, M (μN μm)	418
Drive amplitude, θ_z (°)	0.305

Table 3
The characteristics of the dual-axis sensing modes and the associated dynamic performances

Design parameter	Ω_x sensing-axis	Ω_y sensing-axis
Dynamic range	±150°/s	±150°/s
Nonlinearity	0.29%	0.04%
Natural frequency	ω_y: 4606 Hz	ω_x: 4604 Hz
dc Tuning voltage	54 V	42 V
Coriolis torque	0.33 μN μm/°/s	0.03 μN μm/°/s
Sensitivity	0.00076°/°/s	0.00083°/°/s
	0.018 μm/°/s	0.0086 μm/°/s
	19.4 fF/°/s	7.4 fF/°/s

4. Conclusions

The design considerations, operation principle, mathematical model governing dynamic characteristics and simulation for a novel dual-axis sensing decoupled vibratory wheel gyroscope were presented. The presented design not only prevents the sensing coupled problem, but also provides the capability to measure the dual-axis angular rates. Triple-beam-shape torsional spring within the device was used to suppress the undesired in-plane linear motion of the outer-ring. The feasibility of the present study has been demonstrated by the performance of the dual-axis gyroscope in Table 1. The simulation results show that the natural frequencies of the driving mode and the dual-axis sensing modes are 4585, 4604 and 4606 Hz, respectively. With the dc tuning voltages of 42 and 54 V, respectively, the frequencies of the dual-axis sensing modes are identical with the driving one. With the driving voltage of 20 V and the quality factor of 2000, the sensitivities of the dual-axis sensing modes can reach 7.4 and 19.4 fF/°/s, respectively, and the nonlinearity of the dual-axis sensing modes are only 0.04 and 0.29% within the sensing range of ±150°/s. It successfully demonstrates that the dual-axis sensing modes are decoupled.

Acknowledgements

This project was (partially) supported by National Science Council, Taiwan under Contract No. NSC 94-2218-E-007-028. The authors would like to appreciate the National Science Council Central Regional MEMS Research Center (Taiwan), Nano facility Center of National Chiao-Tung University (Taiwan), and National Nano Device Laboratory (Taiwan), in providing the fabrication facilities.

References

[1] K. Funk, H. Emmerich, A. Schilp, M. Offenberg, R. Neul, F. Larmer, A surface micromachined silicon using a thick polysilicon layer, in: Proceedings of the IEEE MEMS'99, Orlando, FL, January 1999, pp. 57–60.
[2] S. An, Y.S. Oh, K.Y. Park, S.S. Lee, C.M. Song, Dual-axis microgyroscope with closed-loop detection, Sens. Actuators A 73 (1999) 1–6.
[3] T. Fujita, K. Maenaka, T. Mizuno, T. Matsuoka, T. Kojima, T. Oshima, M. Maeda, Disk-shaped bulk micromachined gyroscope with vacuum sealing, Sens. Actuators A 82 (2000) 198–204.
[4] T. Fujita, K. Maenaka, M. Maeda, Design of two-dimensional micromachined gyroscope by using nickel electroplating, Sens. Actuators A 66 (1998) 173–177.
[5] T.K. Tang, R.C. Gutierrez, C.B. Stell, V. Vorperian, G.A. Arakaki, J.T. Rice, W.J. Li, I. Chakraborty, K. Shcheglov, J.Z. Wilcox, W.J. Kaiser, A packaged silicon MEMS vibratory gyroscope for microspacecraft, in: Proceedings of the IEEE MEMS'97, Nagoya, Japan, January1997, pp. 500–505.
[6] T. Juneau, A.P. Pisano, J.H. Smith, Dual axis operation of a micromachined rate gyroscope, in: Proceedings of the Transducers'97, Chicago, IL, June 1997, pp. 883–886.
[7] W. Geiger, W.U. Butt, A. Gaißer, J. Frech, M. Braxmaier, T. Link, A. Kohne, P. Nommensen, H. Sandmaier, W. Lang, Decoupled microgyros and the design principle DAVED, Sens. Actuators A 95 (2002) 239–249.
[8] Multi-element micro gyro, US Patent 5,955,668 (1999), Irvine Sensors Corporation, Costa Mesa, CA.
[9] Electrically decoupled micromachined gyroscope, WO 01/20259 A1 (2001), Kionix, Inc.
[10] Silicon gyro with integrated driving and sensing structure, US Patent 6374672 B1 (2002), Litton System Inc., Woodland Hills, CA.
[11] M. Palaniapan, R.T. Howe, J. Yasaitis, Performance comparison of integrated *Z*-axis frame microgyroscopes, in: Proceedings of the IEEE MEMS'03, Kyoto, Japan, January 2003, pp. 482–485.
[12] Gyroscope, US Patent 6343509 B1 (2002), BAE System PLC, Hants (GB).
[13] Guohong He, K. Najafi, A single-crystal silicon vibrating ring gyroscope, in: Proceedings of the IEEE MEMS'02, Las Vegas, NV, January 2002, pp. 718–721.
[14] F. Ayazi, K. Najafi, A HARPSS polysilicon vibrating ring gyroscope, J. Microelectromech. Syst. 10 (2001) 169–179.
[15] E. Boser, Electronics for micromachined inertial sensors, in: Proceedings of the Transducers'97, Chicago, IL, June 1997, pp. 1169–1172.
[16] Y. Mochida, M. Tamura, K. Ohwada, A micromachined vibrating rate gyroscope with independent beams for the drive and detection modes, Sens. Actuators A 80 (2000) 170–178.

Biographies

Deng-Horng Tsai received his B.S. degree in mechanical engineering from National Chung Hsing University, Taiwan in 1986 and M.S. degree in aeronautics and astronautics from National Cheng Kung University, Taiwan in 1988. Then, he has been working in Chung-Shan Institute of Science and Technology ever since. He is currently studying for his Ph.D. degree at the Department of Power Mechanical Engineering, National Tsing Hua University, Taiwan. His current research interest is in micromachined inertial sensors.

Weileun Fang received his Ph.D. degree from Carnegie Mellon University in 1995. His doctoral research focused on the determining of the mechanical properties of thin films using micromachined structures. In 1995, he worked as a postdoctoral research at Synchrotron Radiation Research Center, Taiwan. He is currently a professor at Power Mechanical Engineering Department and MEMS Institute, National Tsing Hua University, Taiwan. His research interests include MEMS with emphasis on novel microfabrication process, microoptical systems, microactuators, and the characterization of the mechanical properties of thin films.